

Nanopore-Based Power Generation from Salinity Gradient: Why It Is Not Viable

Li Wang, Zhangxin Wang, Sohum K. Patel, Shihong Lin, and Menachem Elimelech*

Cite This: *ACS Nano* 2021, 15, 4093–4107

Read Online

ACCESS |

Metrics & More

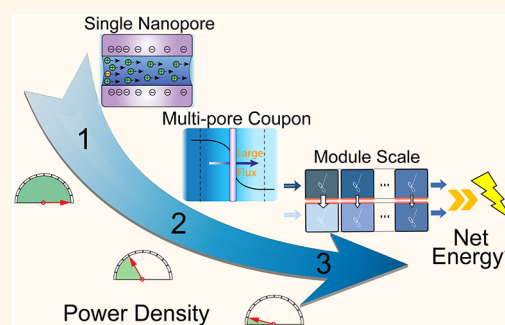
Article Recommendations

Supporting Information

ABSTRACT: In recent years, the development of nanopore-based membranes has revitalized the prospect of harvesting salinity gradient (blue) energy. In this study, we systematically analyze the energetic performance of nanopore-based power generation (NPG) at various process scales, beginning with a single nanopore, followed by a multipore membrane coupon, and ending with a full-scale system. We confirm the high power densities attainable by a single nanopore and demonstrate that, at the coupon scale and above, concentration polarization severely hinders the power density of NPG, revealing the common, yet significant, error in linearly extrapolating single-pore performance to multipore membranes. Through our consideration of concentration polarization, we also importantly show that the development of materials with exceptional nanopore properties provides limited enhancement of practical process performance.

For a full-scale NPG membrane module, we find an inherent tradeoff between power density and thermodynamic energy efficiency, whereby achieving a high power density sacrifices the energy efficiency. Furthermore, we derive a simple expression for the theoretical maximum energy efficiency of NPG, showing it is solely related to the membrane selectivity (*i.e.*, $S^2/2$). Through this relation, it is apparent that the energy efficiency of NPG is limited to only 50% (for a completely selective membrane, *i.e.*, $S = 1$), reinforcing our optimistic full-scale simulations which result in a (practical) maximum energy efficiency of 42%. Finally, we assess the net extractable energy of a full-scale NPG system which mixes river water and seawater by including the energy losses from pretreatment and pumping, revealing that the NPG process—both in its current state of development and in the case of highly optimistic performance with minimized external energy losses—is not viable for power generation.

KEYWORDS: salinity gradient energy, nanopore, power generation, multiscale modeling, power density, energy efficiency



Climate change—accelerated by humanity’s widespread reliance on fossil fuels—continues to progress at an alarming rate. In an effort to minimize adverse environmental impact, while sustaining the growing energy demands of modern society, alternative energy sources are extensively explored. The past decades have increasingly focused on harvesting the “blue” energy from the mixing of waters with differing salinities. Specifically, when solutions of varying chemical potential are mixed, the Gibbs free energy of mixing is released, which can be utilized to perform useful work. Blue energy has enormous potential, with studies predicting that thousands of terawatt hours of energy are available to be harnessed from the mixing of river waters and seawater.^{1–5} Such a tremendous amount of energy would be sufficient for satisfying much of humanity’s energy requirements and is even greater than combining the potential energy of many marine-based energy sources including tides, waves, and currents.¹

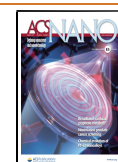
Several technologies have been developed to harvest blue energy, among which pressure-retarded osmosis (PRO) and

reverse electrodialysis (RED) are the most heavily investigated.^{6,7} Both being membrane-based processes, PRO and RED rely on the selective transport of water and salt ions, respectively. In PRO, a semipermeable membrane separates a low-salinity solution from a high-salinity (draw) solution.^{8–10} The membrane, being permeable to water molecules but not salt ions, enables osmosis to offset the chemical potential difference between the solutions. As water traverses the membrane from the low-salinity side to the high-salinity side, the hydrostatic pressure in the high-salinity reservoir builds and can be converted to electric power by passing the pressurized water through a turbine. RED, in contrast to PRO, transports salt ions from a high-salinity to low-salinity reservoir

Received: October 15, 2020

Accepted: January 21, 2021

Published: January 26, 2021



to balance the chemical potential.^{11,12} Ion-exchange membranes (IEMs), which preferentially transport counterions (*i.e.*, species with charge opposite of the IEM), facilitate the transport of anions and cations in opposite directions, thus generating an ionic current. The ionic current can readily be converted to an electrical current by placing electrodes at the two ends of an IEM stack, at which reversible redox reactions occur.

Investigation of PRO and RED has primarily been at the coupon scale, just recently having been demonstrated at a more sizable operation. Bench-scale PRO with coupon-scale membranes has generated power densities up to 9 W m⁻² when synthetic seawater was used as the draw solution,^{13–15} and studies focused on membrane development and underlying transport phenomena have shown less tortuous and more porous support layers are key factors for improving the power density. The power densities of bench-scale RED have remained notably lower than those of PRO (<4 W m⁻²), with researchers finding the intermembrane distance to be a critical parameter in optimizing the power density.¹⁶ Despite tremendous research efforts, PRO and RED have thus far failed to achieve sufficiently high power densities at full scale, limiting their widespread application. Specifically, the first full-scale PRO plant reported power densities within 3–3.7 W m⁻²,¹⁷ whereas a pilot-scale RED plant demonstrated a power density of only 1.6 W m⁻² by mixing brackish water and concentrated brine.¹⁸ Scale-up of PRO and RED systems is further complicated by an inherent tradeoff between the extractable energy and the power density.^{10,12,19–21} According to this tradeoff, the largest power densities are obtained when the solution mixing, and thus the harvested energy, are minimized—counterproductive conditions toward achieving feasible operation. However, even when disregarding power density and focusing solely on maximizing the solution mixing and harvested energy, the viability of PRO and RED has faced scrutiny due to the relatively low maximum energy of extraction.^{22,23}

Nonetheless, RED, in particular, has increasingly attracted research attention over recent years due to advancements in the material fabrication of ion-selective membranes.^{24–28} A wide range of advanced materials have been demonstrated for harnessing blue energy, including solid-state metal oxides,^{29–33} polymers,^{34–38} metal–organic frameworks,³⁹ and hybrid composites.^{40–44} Low-dimensional materials have been considered particularly promising due to reportedly high ionic conductance and selectivity.^{45–51} For instance, nanoconfined boron nitride nanotubes (BNNTs) with high surface charge density were synthesized, achieving a power density of 4 kW m⁻² with a single nanopore.⁴⁹ More recently, porous single-layer molybdenum disulfide (MoS₂) showed extremely high conductance owing to its atomic-level thickness and attained a power density of 10³ kW m⁻² for a single nanopore.⁴⁸ Thus, the application of nanochannels for harvesting blue energy has attracted considerable attention, developing into its own highly researched field termed nanopore-based power generation (NPG).^{52–54}

The extremely high power densities demonstrated with a single nanopore by NPG intuitively suggest significant performance enhancement over traditional ion-exchange membrane-based RED. However, it is critical to note that investigation thus far has been limited to the bench scale under ideal experimental conditions. Consideration of nanopore-based membranes rather than a single nanopore, their

application to full-scale systems, and the impact of full-scale operation on process performance have remained largely unexplored. Specifically, assessment of NPG's net energy efficiency and inherent limitations, particularly at full process scale and with realistic operating conditions, is essential toward determining the practical significance of advancing nanopore materials for power generation.

In this paper, we systematically assess the viability of nanopore-based power generation over multiple process scales (Figure S1). Starting with a single ion-selective nanopore, we describe the mechanism of harvesting salinity gradient energy and quantify the effects of pore selectivity and conductance on power generation. Through rigorous modeling, we demonstrate that the power produced by a single nanopore can be extremely high, as reported in the literature. We then model a coupon-scale element of a multipore membrane, revealing significant loss in power generation compared to a single pore due to the detrimental effects of concentration polarization. Next, we extend our modeling to the module scale, through which we show a critical tradeoff between the thermodynamic energy efficiency and the power density. Finally, we consider the case of a practical nanopore-based power generation system—mixing river water with seawater—to evaluate if net electricity can be produced when also accounting for the energy demand of pumping and pretreatment processes.

RESULTS AND DISCUSSION

A typical batch-operated NPG system consists of two solutions of different salinities separated by an ion-selective membrane composed of charged nanopores (Figure 1). Due to the transmembrane concentration gradient, salt ions diffuse across the membrane nanopores from the concentrated solution to the dilute solution. The membrane, here assumed to be negatively charged (as is typical of NPG systems), preferentially transports cations over anions, thus generating an ionic charge flux (the difference between the cationic and anionic fluxes). As a result of the charge flux, an electrical potential difference, commonly termed the membrane potential (ΔE_m), arises across the membrane.

The membrane potential can be approximated by the Nernst equation:^{12,29}

$$\Delta E_m = S \frac{RT}{zF} \ln \frac{c_H}{c_L} \quad (1)$$

where R is the gas constant, T is the absolute temperature, z is the ion valence, S is the selectivity, and c_H and c_L are the molar salt concentrations at the membrane surface in the high- and low-salinity solution sides, respectively. We note that a more accurate expression of eq 1 should use ion activity instead of the molar concentration of the ions. However, in this analysis, we assume ideal solutions for which molar concentrations equal activity. The selectivity in eq 1 is defined as the ratio of the ionic charge flux to the total salt flux, and can be expressed for a negatively charged nanopore as⁵⁵

$$S = \frac{J_+ - J_-}{J_+ + J_-} \quad (2)$$

where J_+ and J_- are the cationic and anionic fluxes, respectively. For a perfectly selective nanopore, which completely prevents co-ion passage, the selectivity is unity. In contrast, for an uncharged nanopore that does not distinguish between the

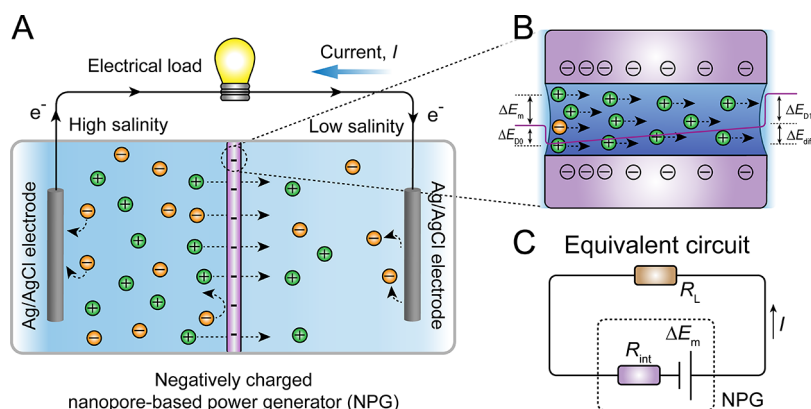


Figure 1. Harvesting of electrical energy *via* a nanopore power generator (NPG) membrane. (A) Schematic illustration of harvesting energy from salt concentration gradient *via* a nanopore-based power generator. A selective membrane favors the transport of counterions from the high-concentration reservoir (left) to the low-concentration reservoir (right) and thus generates an ionic current. A negatively charged membrane, which favors the flux of cations over anions, is shown. The difference between the cationic flux and anionic flux is the ionic current, I . The reference electrodes are necessary to convert the ionic current to electrical current *via* redox reactions, thereby closing the electrical circuit. (B) Counter- and co-ion transport in a charged nanopore under a concentration gradient. The total ion concentration at the pore inlet (left side) is higher than that at the pore outlet (right side). As a result, the membrane potential, ΔE_m , rises from left to right, as shown in the schematics. The Donnan potentials (ΔE_{D0} and ΔE_{D1}), established at the nanopore-solution interfaces, together with the transpore diffusion potential (ΔE_{diff}), constitute ΔE_m . (C) Equivalent circuit representing the harvesting of energy by an external load, R_L , where R_{int} is the internal resistance of the nanopore-based power generator.

transport of counterions and co-ions, both the selectivity and membrane potential are zero.

Though useful for approximating the membrane potential, eq 1 neglects several fundamental ion transport phenomena. As shown in Figure 1B, the membrane potential, ΔE_m , has three contributions: the Donnan potentials at each edge of the nanopore (*i.e.*, ΔE_{D0} and ΔE_{D1}) and the diffusion potential (ΔE_{diff}) across the nanopore:^{56,57}

$$\Delta E_m = -\Delta E_{D0} + \Delta E_{diff} + \Delta E_{D1} \quad (3)$$

At the high-salinity side, the pore's negative charge is more effectively screened; thus, the magnitude of the Donnan potential on the high-salinity side, ΔE_{D0} , is smaller than that on the low-salinity side, ΔE_{D1} . As a result of the transpore concentration gradient and the greater mobility of cations over anions, a potential difference, namely, the diffusion potential, arises along the pore.⁵⁸ Specifically, with the high-salinity end of the pore containing a higher cation concentration than the low-salinity end, the potential across the pore gradually increases. Similarly, proton concentration variation across the pore also contributes to the potential rise,⁵⁶ with a more detailed explanation of the pH gradient across the pore and its effects provided in the Methods section.

As cations selectively cross the nanopore and accumulate in the low-salinity reservoir, anions remain in the high-salinity reservoir. To ensure charge neutrality, a pair of redox electrodes (*e.g.*, Ag/AgCl) are employed. Redox reactions at the electrodes also enable the conversion of the ionic charge flux into an electrical current, thereby completing the electrical circuit.

Maximum Power Density in NPG Depends on Pore Conductance and Selectivity. Energy is harvested by connecting the electrodes in the reservoirs to an external load with a resistance of R_L , as shown by the equivalent circuit in Figure 1C. The power of the NPG system, P , is given by

$$P = I^2 R_L \quad (4)$$

where I is the current. The maximum power, P_{max} , is achieved when the external load resistance is nearly equal to the internal resistance of the membrane, R_{int} , which can be expressed as^{29,59}

$$P_{max} = \frac{\Delta E_m^2}{4R_{int}} = \frac{\Delta E_m^2 G_{int}}{4} \quad (5)$$

where G_{int} is the internal conductance. The maximum power is therefore a function of the membrane potential and the internal conductance of the membrane. As the membrane potential is dependent on the pore selectivity according to eq 1, a membrane with both high selectivity and conductance is highly desirable.^{53,54,60} We note that selectivity and conductance are determined by intrinsic pore properties, including the areal density of functional groups on the pore wall and their degree of dissociation,^{61–64} as well as the pore size^{48,65,66} and length.^{48,55,67}

The areal density and dissociation constant of the functional groups on the pore wall are critical parameters as they ultimately determine the pore surface charge. It has been verified by theoretical and experimental studies that weak acid equilibrium with one dissociation constant (pK_a) is sufficient for describing the dependence of surface charge density on pH for a wide range of charged nanopores.^{49,62,68–74} For a constant pH, a lower pK_a results in a higher degree of deprotonation of the functional groups and thus greater pore charge density. Increasing the areal density of the dissociable groups also yields a larger charge density. Specifically, the pore wall surface charge density (σ) is dependent on the areal density of the functional groups (N), the solution pH, and the acid dissociation constant (pK_a) by⁶²

$$\sigma = -e \frac{N}{1 + 10^{pK_a - pH}} \quad (6)$$

where e is the elementary charge. A higher surface charge enables greater repulsion of co-ions and a faster rate of counterion passage, thus enhancing pore selectivity and conductance, respectively. Though surface charge has clear dependence on the acid dissociation constant and the areal

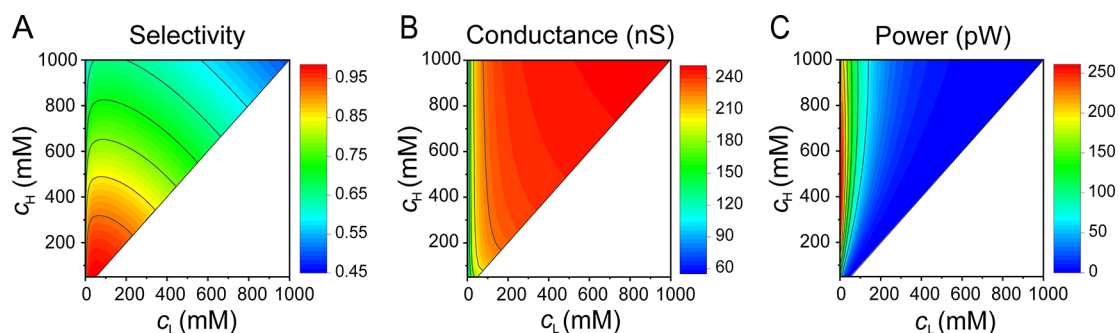


Figure 2. (A) Selectivity, (B) conductance, and (C) maximum power of a single nanopore as a function of the concentrations of the high-salinity solution, c_H , and low-salinity solution, c_L . The modeled pore diameter is 10 nm; the number of dissociable sites is 5.3 nm^{-2} ; the $\text{p}K_a$ is 8.9, and the solution pH is 11. The parameters used in the calculations, including the solution pH and pore diameter, are similar to those reported for a MoS_2 single nanopore (ref 48). The dissociable site density and the $\text{p}K_a$ are the best fitted values.

density of the functional groups, the most practical method for tuning the pore charge density for a given membrane is by increasing the solution pH, as shown in Figure S2.

The pore size and length also influence the selectivity and conductance. Decreasing the pore size leads to greater overlap of the electrical double layers (EDLs), which increases the magnitude of the electric potential in the pore.^{75,76} A smaller pore size also effectively increases the volumetric charge density within the pore.⁷⁷ Thus, a smaller pore size (with enhanced EDL overlap and volumetric charge density) results in a higher selectivity. The conductance, however, decreases with shrinking pore size due to the combined effect of decreased ionic flux (caused by a smaller cross-sectional area of the pore) and increased voltage (decreasing pore size increases selectivity).^{48,53} Therefore, considering this tradeoff between the selectivity and conductance, the pore size must be carefully optimized to maximize power generation. The optimal pore size for an MoS_2 nanopore used in a recent NPG study has been experimentally identified as ~ 10 nm for concentrations of 1000 and 1 mM for the high- and low-salinity solutions, respectively.⁴⁸ Note that the optimal pore size is dependent on the solution concentrations on both sides of the charged nanopore, decreasing in value as the concentration ratio increases (Figure S3). Decreasing the pore length is also beneficial to the power generation through enhancement of the pore conductance.⁵⁴ Specifically, with a shorter pore length, the transpore concentration gradient increases, enhancing the rate of ion transport and thus the pore conductance.

A tremendous amount of effort has been directed toward increasing the pore selectivity and conductance through the aforementioned approaches of tuning surface functional groups, pore size, and pore length (details in Table S1).^{27,32–35,40–46,48–51,78,79} According to the analysis presented thus far, these efforts are seemingly logical approaches to enhancing NPG performance. However, the validity and limitations of these approaches when extended beyond a single nanopore (*i.e.*, to a multipore membrane coupon or a membrane module) has remained largely uninvestigated.

A Single Nanopore Can Generate Ultrahigh Power.

We begin our systematic analysis with a single nanopore to confirm and provide further insight into expected NPG performance trends. Our simulations throughout this study are based on a validated ion transport model, with further details of the model derivation provided in the Methods section. The model has been validated with a wide range of experimental data collected from the NPG literature under

different salinity gradients, solution pH, and nanopore sizes (Figure S2). As previously discussed, the generated power in NPG is dependent on the pore size, pore length, and surface functional groups. However, it has also been experimentally demonstrated that the pore selectivity and conductance are strongly affected by the solution concentrations at the two ends of the nanopore.²⁹ Here, we analyze the effect of various salinity gradients on the selectivity, conductance, and the corresponding maximum power of a single nanopore (as given by eq 5).

As shown in Figure 2A, the selectivity is maximized when the salt concentrations on both sides of the pore are relatively small (*i.e.*, less than ~ 100 mM). When the solution concentrations are increased, the selectivity significantly deteriorates due to EDL compression (*i.e.*, less EDL overlap) at high ionic strength. Pore conductance, in contrast, increases with solution concentration (Figure 2B). Specifically, the pore wall surface charge is effectively screened by a solution of high salinity, leading to a reduction of electric potential within the pores and thus a decline in selectivity. Furthermore, as salt concentration is increased at the pore inlet, large transpore concentration gradients (of both the counter- and co-ions) are generated. Though this enhances the rate of ion transport through the pore—and hence the pore conductance—the increased co-ion concentration gradient exacerbates co-ion transport, thus sacrificing selectivity. Consequently, a tradeoff between the selectivity and conductance exists, apparent upon comparing Figure 2A,B.^{29,80}

The maximum power for the single nanopore is determined by eq 5 and shown in Figure 2C. Generally, when the salt concentration of the low-salinity reservoir is within the brackish water range (*i.e.*, less than ~ 100 mM), the single-pore power approaches 250 pW, in close agreement with the experimental results of an MoS_2 nanopore which achieved up to 233 pW.⁴⁸ Instead of reporting the power, however, it is more insightful to use power density as a performance metric, as it is inherently related to the size of the pore or membrane area (for multipore membrane studies). Two methods are often adopted to calculate the power density: normalization of the power by the cross-sectional area of the pore or normalization by the total membrane area (which requires knowledge of the number density of pores per membrane area). With both methods, the power densities reported are on the order of 10^6 W m^{-2} .^{48,49} However, it is critical to note that neither approach is sufficient for predicting the performance of

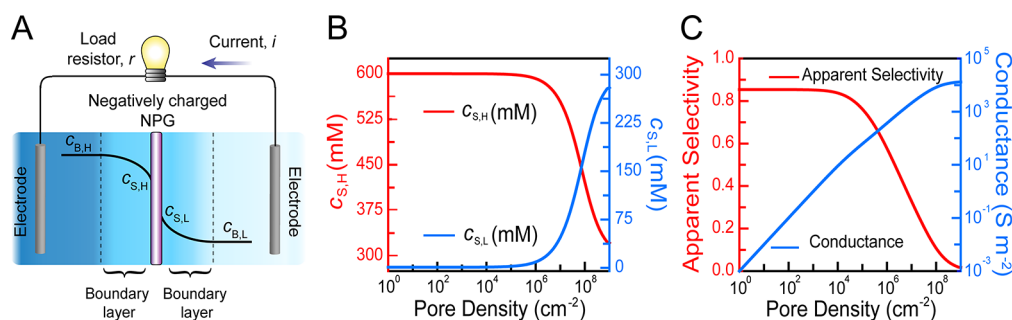


Figure 3. Significance of concentration polarization for a multipore membrane coupon. (A) Schematic representation of concentration polarization as a result of large salt flux, J_{salt} . Concentration polarization reduces the transmembrane concentration difference, and consequently the membrane potential decreases. (B) Solution concentrations at the membrane surface change as the pore density increases due to concentration polarization. High pore density leads to a large salt flux, which decreases the solution concentration at the membrane surface on the high-salinity side, $c_{s,H}$, and increases the solution concentration at the membrane surface on the low-salinity side, $c_{s,L}$. (C) Dependence of apparent selectivity and membrane conductance on pore density when considering concentration polarization. The following conditions are used in the simulations: boundary layer thickness of $50 \mu\text{m}$ (assuming steady state and no chemical reactions), $\text{p}K_a$ of 4, dissociable charge site density of 4 nm^{-2} , membrane thickness of 6.5 nm , cylindrical nanopores with a diameter of 10 nm , pH 7, and salt concentrations of 600 and 1 mM for the high- and low-salinity solution, respectively.

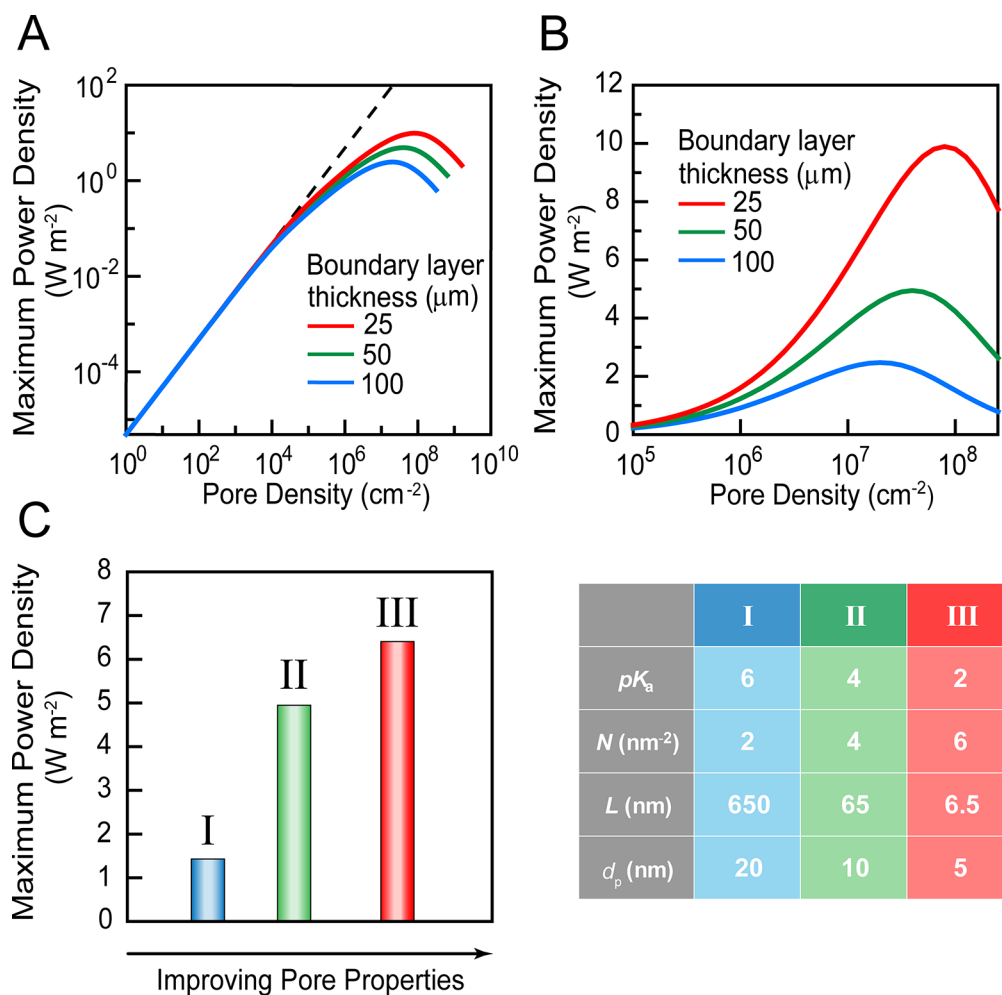


Figure 4. Power density is drastically reduced by concentration polarization. (A) Maximum power density as a function of pore density for different boundary layer thicknesses. The dashed line represents an ideal linear extrapolation of power density with pore density. (B) Zoom-in of the power density in the range of pore density from 10^5 to $2.5 \times 10^8 \text{ cm}^{-2}$. (C) Impact of pore properties on maximum power density for three cases (described in the legend on the right) with different $\text{p}K_a$, dissociable site density of functional groups (N), membrane thickness (L), and pore size (d_p). When modeling (A), the thickness of the multipore membrane is 6.5 nm , pore diameter is 10 nm , dissociable site density is 4 nm^{-2} , $\text{p}K_a$ is 4, solution pH is 7, and salt concentrations are 600 and 1 mM for the high and low-salinity side, respectively. In (C), specific pore properties are listed in the table, and the boundary layer thickness is set as $50 \mu\text{m}$ for all three cases.

a practical NPG system composed of a multipore membrane as we discuss in the next section.

Concentration Polarization Is Inherent in Multipore NPG. In this section, we show why a simple linear extrapolation is erroneous for scaling the performance of a single nanopore to a multipore membrane by analyzing a coupon-scale element of a nanopore-based membrane. For a membrane with a given area, increasing the number of nanopores per area leads to a larger ionic flux. As the ionic flux through the membrane increases, the salt concentration near the membrane surface facing the concentrated solution is reduced compared to that of the bulk solution. The opposite occurs in the low-salinity reservoir, where the transmembrane ionic flux results in an increased concentration near the membrane surface as compared to the bulk (Figure 3A). This phenomenon is known as concentration polarization and is inherent of all membrane separation processes.^{81–85}

To demonstrate the importance of concentration polarization in power generation with a multipore membrane, we simulate the energy generation from the controlled mixing of seawater (600 mM) and fresh water (1 mM). It is clear that concentration polarization begins to drastically affect the solution concentrations near the membrane surfaces when the pore density increases beyond $\sim 10^6 \text{ cm}^{-2}$ (Figure 3B). Concentration polarization, which is modeled according to the film theory (with the assumptions of steady state and no chemical reactions) results in a lower transpore concentration gradient, decreasing the driving force for diffusive transport and hence reducing the practical membrane potential (ΔE_m^{cp}). The apparent membrane selectivity—the ratio of the actual membrane potential to the ideal membrane potential (in the absence of concentration polarization)—can be calculated according to the following equation:

$$S_{\text{app}} = \frac{\Delta E_m^{\text{cp}}}{\frac{RT}{zF} \ln \frac{c_H}{c_L}} \quad (7)$$

In Figure 3C, the apparent selectivity is shown to rapidly decline above pore densities of $\sim 10^4 \text{ cm}^{-2}$, eventually approaching zero as the result of severe concentration polarization. In contrast, the intrinsic selectivity, which is dependent on the concentration of the solutions in contact with the membrane coupons, increases as a result of concentration polarization (Figure S4).

The conductance of the membrane coupon is also negatively impacted by concentration polarization. As previously discussed, concentration polarization results in a lower salt concentration at the membrane surface facing the concentrated solution compared to that of the bulk, while the opposite phenomenon occurs in the dilute solution side. Due to the lower salt concentration at each pore entrance and the reduced transmembrane driving force, fewer ions are transported through the individual pores, resulting in a decrease of the ionic conductance per pore. Consequently, increasing the pore density does not linearly enhance the overall membrane conductance (Figure 3C).

Concentration Polarization Dramatically Reduces the Power Density of Multipore NPG. With concentration polarization compromising the membrane selectivity and conductance, the maximum power density also deteriorates, deviating significantly from the case of simple linear extrapolation as pore density exceeds a critical value— 10^4 cm^{-2} for the case simulated (Figure 4A). Above this critical

pore density, the rate of increase in maximum power density with respect to the pore density diminishes, ultimately reaching a peak value before declining. In the case of very large pore densities, the membrane potential approaches zero because of severe concentration polarization. Though the membrane is still able to maintain a relatively high conductance, the small membrane potential ultimately undermines the power density. The detrimental effect of high pore density on power density has also been observed in previous studies.^{52,86}

The extent of concentration polarization can be minimized by decreasing the boundary layer thickness through enhanced hydrodynamic conditions. A thinner boundary layer yields larger maximum power density across the high pore density range (Figure 4B). For instance, when the boundary layer thickness decreases from 100 to 25 μm , the peak value of the maximum power density increases from 2.47 to 9.89 W m^{-2} . The pore density corresponding to the peak power density is also related to the boundary layer thickness. For a smaller boundary layer thickness, the maximum power density is observed at a higher pore density.

Ongoing efforts primarily aim to improve NPG performance by enhancing pore properties, though little theoretical analysis has been conducted beyond a single nanopore. Here, we evaluate the potential of improved pore properties in augmenting the maximum power density for a coupon-scale membrane. As previously discussed for a single nanopore, a short pore with high surface density of functional groups and a small $\text{p}K_a$ for those dissociable functional groups is favorable for enhancing pore selectivity and conductance.^{70,87,88} These conclusions remain valid for a multipore membrane. The effects of pore size, however, are more complex at the coupon-scale than for a single nanopore due to concentration polarization. The previously highlighted tradeoff by which decreasing pore size results in higher selectivity at the expense of lower conductance persists at the coupon-scale. However, for a fixed pore density, as the pores become smaller and ionic flux per pore is reduced, concentration polarization and its detrimental impact on performance are effectively mitigated. Therefore, the enhancement of power density from reduction in the pore size is more significant for a coupon-scale membrane than for a single nanopore.

In Figure 4C, we progressively enhance each of the pore properties over three scenarios, revealing that the pore properties are relevant to process performance only up to a limit. Enhancing the properties from condition I to II results in considerable increase in maximum power density, while further enhancement from condition II to III demonstrates diminishing returns toward increasing power density. A detailed sensitivity analysis, in which each of the pore properties is systematically varied, is provided in Figure S5 and shows that the pore size is the most effective property to manipulate for improving the power density.

Maximum Extractable Energy at the Module (System) Scale Is Limited by the Gibbs Free Energy of Mixing. As demonstrated by our coupon-scale analysis, the performance of a multi-nanopore membrane significantly deviates from that of a single nanopore. However, to better represent realistic NPG operation and performance, we further extend our evaluation from the coupon scale (relevant to bench-scale experiments) to a full membrane module (representative of full-scale NPG systems). The module-scale analysis is performed on an NPG system operated in batch mode, as has been demonstrated by previous studies.^{12,89}

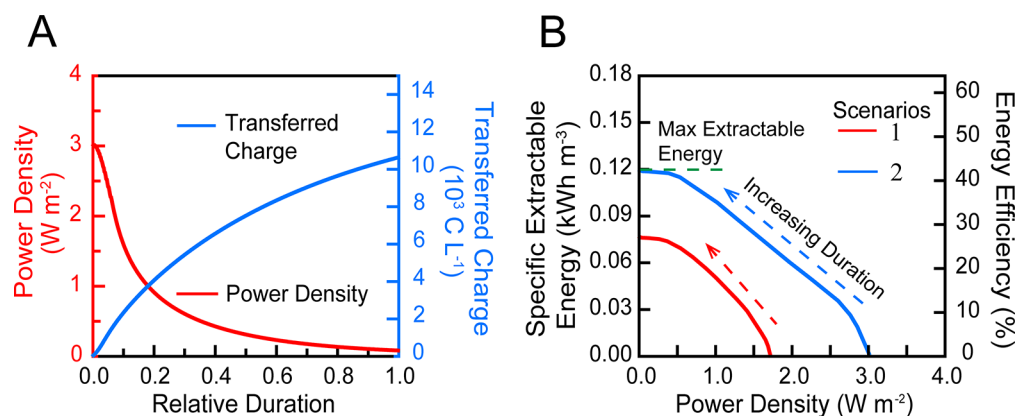


Figure 5. Module-scale analysis for nanopore-based power generation. (A) Variation of power density and transferred charge as a function of the relative duration (t/τ). A relative duration of 0 refers to an infinitesimally short batch duration ($t = 0$), while 1.0 refers to the ultimate duration ($t = \tau$), defined as the time required to achieve 95% of complete solution mixing. Power density decreases with relative duration due to the decreasing driving force (or concentration difference across the membrane) as the solutions at the two sides of the membrane continuously mix to extract energy. (B) Tradeoff between extractable energy and power density at the module scale. Power density decreases with increasing duration of batch operation, while extractable energy increases due to increased solution mixing (or charge transfer) across the membrane. The extractable energy is expressed as the energy extracted per total volume of the high- and low-concentration solutions. The energy efficiency is defined as the extractable energy divided by the Gibbs free energy of mixing. Two scenarios (1 and 2) are modeled, both of which use a dissociable site density of 4 nm^{-2} and a $\text{p}K_a$ of 4. In scenario 1, the pore density is $5 \times 10^6 \text{ cm}^{-2}$, the nanopore diameter is 10 nm, and the boundary layer thickness is $77 \mu\text{m}$. Considerably more favorable conditions are simulated by scenario 2 in which the pore density is 10^8 cm^{-2} , the nanopore diameter is 2 nm, and the boundary layer thickness is $25 \mu\text{m}$. The high-concentration solution (600 mM) and the low-concentration solution (1 mM) flow concurrently along the membrane module and are continuously recirculated for the duration of the batch. The flow velocity is varied to attain the specified boundary layer thickness. The pH of both solutions is 7, and the spacer channel thickness of the module is 0.3 mm.

Specifically, both the high- and low-salinity solutions are passed concurrently along the membrane and continuously recirculated over the duration of the batch (Figure S6). As the solutions are recirculated, salt diffuses across the membrane, resulting in gradual solution mixing and energy extraction. For such operation, it is necessary to account for the temporal variation in the salinity of both solutions. As solution mixing or energy extraction progresses, salt flux across the membrane results in the dilution of the high-salinity solution and concentration of the low-salinity solution, thus reducing the membrane potential across the membrane.

The theoretical maximum extractable energy from the mixing of the high and low-salinity solutions is limited by the Gibbs free energy of mixing.^{10,77} The Gibbs free energy of mixing can only be obtained in the case where the extraction process is operated in a thermodynamically reversible manner. However, a thermodynamically reversible process is impractical and only theoretically possible in batch mode, with a variable external load resistance which continuously maintains a voltage drop across the load that is infinitesimally smaller than the membrane potential. The Gibbs free energy of mixing normalized by the total volume of the solutions gives the specific Gibbs free energy of mixing, ΔG_{mix} which can be expressed as^{90,91}

$$\Delta G_{\text{mix}} = \nu RT \{ c_M \ln(c_M) - \gamma c_H \ln(c_H) - (1 - \gamma) c_L \ln(c_L) \} \quad (8)$$

where ν is the van't Hoff factor ($\nu = 2$ for a fully dissociated monovalent salt), γ is the volume ratio of the high-salinity solution over the total volume of both solutions, and c_M is the final concentration of the mixed solution. In the following analysis, γ is fixed at 0.5 (*i.e.*, the volumes of the high-salinity and the low-salinity solutions are equal). We note that γ affects the extractable energy and power density, though the

optimization of the volume ratio is outside of the scope of this study.

In a practical NPG module, not all of the Gibbs free energy of mixing is extractable, as losses associated with entropy generation due to finite kinetics of mixing are inevitable. The extractable energy normalized by the total volume of the solutions (V_{tot}) is termed the specific extractable energy (*SEE*) and is determined by integrating the membrane potential with respect to transferred charge (Q) throughout the membrane module:

$$SEE = \frac{\int_0^{Q_f} \Delta E_m dQ}{V_{\text{tot}}} \quad (9)$$

where Q_f is the cumulative transferred charge at the end of the batch duration. We note that both ΔE_m and Q change as the mixing proceeds and that the extent of mixing is determined by the duration of the batch. Specific extractable energy is particularly useful for direct comparison to the theoretical maximum extractable energy (*i.e.*, the Gibbs free energy of mixing). Particularly, the ratio of the specific extractable energy to the Gibbs free energy of mixing represents the energy efficiency (η) of salinity gradient energy harvesting:

$$\eta = \frac{SEE}{\Delta G_{\text{mix}}} \quad (10)$$

Tradeoff between Extractable Energy and Power Density at the Module Scale. As the extent of solution mixing proceeds with time, the transmembrane concentration gradient in the module diminishes, resulting in a decrease of the charge flux. Therefore, the power density, which is directly related to the charge flux (current density) also decreases with time (Figure 5A), approaching zero for batch durations which are sufficiently long for near complete mixing. To assess the

overall performance of the NPG module, it is useful to quantify the average power density for a batch. The average power density, P_{avg} , is given by the integral of the instantaneous maximum power density, P_{max} , over the total batch duration:

$$P_{\text{avg}} = \frac{\int_0^{\tau} P_{\text{max}} dt}{\tau} \quad (11)$$

where τ is the total duration of the batch process. As a result of the diminishing power density over the duration of the batch, the effective power density obtained at the module scale is significantly smaller than that of the coupon scale. For example, for the case presented in Figure 5A, the power density on the coupon scale is 3.0 W m^{-2} , whereas module-scale operation generates an average power density of only 0.59 W m^{-2} . Though the rate of charge transfer slows down as mixing proceeds, the cumulative transferred charge consistently increases due to the continued mixing of the circulating solutions.

Similar to other membrane-based processes for extracting salinity gradient energy, a tradeoff exists between the specific extractable energy and the power density.^{12,20,21,92} In Figure 5B, the effect of increasing the batch duration on the specific extractable energy, energy efficiency, and power density is shown for two scenarios. In both cases, as the batch duration approaches zero, the specific extractable energy also approaches zero because the extent of solution mixing is negligible; however, a large power density is achieved in this case as a result of the large membrane potential. As the batch duration is increased, the extent of solution mixing and hence the amount of cumulative transferred charge also increases, resulting in enhancement of the specific extractable energy and the energy efficiency. If sufficient operation time is provided, the solutions attain complete mixing and achieve the maximum specific extractable energy and energy efficiency. However, when the two solutions are close to being completely mixed, the membrane potential and the power density approach zero, leading to an overall low average power density.

In scenario 1 of Figure 5B, we simulate conditions representative of the current state of nanopore power generation. The performance of NPG is notably limited for this scenario, achieving a maximum extractable energy and energy efficiency of only 0.077 kWh m^{-3} and 27%, respectively. Upon reducing the boundary layer thickness and considerably improving the nanopore properties from scenario 1 to scenario 2, both the power density and energy efficiency are significantly improved. Nevertheless, the maximum energy efficiency attained—even with the highly optimistic conditions of scenario 2—is still only 42%, revealing the relative inefficiency of NPG compared to other membrane-based energy harvesting processes.^{13,21,22,93}

To further corroborate the low energy efficiency of NPG and highlight the inherent limitations of the process, we compare the thermodynamic equilibrium (ideal) voltage to the practical operating voltage, a method introduced in previous studies to analyze the energy efficiency of electrochemical processes.^{94,95} For the ideal mixing of two monovalent salt solutions, the equilibrium voltage, ΔE_{ideal} , is given by^{94,95}

$$\Delta E_{\text{ideal}} = \frac{2RT}{zF} \ln \frac{c_{\text{H}}}{c_{\text{L}}} \quad (12)$$

The membrane potential (ΔE_{m}), which accounts for nonideal co-ion transport, is scaled down from the ideal potential by the

selectivity coefficient (S). It is also critical to note that in NPG power is harvested from the transport of only one type of ion (cations in our case). Thus, ΔE_{m} is further reduced from ΔE_{ideal} by a factor of 2.

The total charge transferred across the membrane, which is directly related to the extractable energy, also varies between the ideal and practical cases. Specifically, the ratio of the actual transferred charge (Q_{f}) and ideal transferred charge ($Q_{\text{f,ideal}}$) is equivalent to the selectivity coefficient, S . The energy efficiency can thus be expressed as

$$\eta = \frac{\Delta E_{\text{m}} Q_{\text{f}}}{\Delta E_{\text{ideal}} Q_{\text{f,ideal}}} = \frac{S^2}{2} \quad (13)$$

From this relation, it is clear that even with a perfectly selective membrane, the energy efficiency of NPG is limited to 50%. For practical systems, which require operation at nonzero power density, the selectivity is sacrificed and energy efficiencies less than 50% are expected. For example, in the highly optimistic scenario 2 of Figure 5B, the energy efficiency achieved for a power density of 1.5 W m^{-2} (half of the maximum power density) is only 28%. Therefore, development of an anion-selective NPG membrane is imperative to enhance the energy efficiency, though it is important to note that incorporation of the additional membrane would effectively halve the power density. We note that the fabrication of anion-selective nanoporous membranes is still under development and is considered to be highly challenging.⁵³ In the case an effective anion-selective NPG membrane could be realized, the NPG process would closely resemble the well-established RED—both in design and expected energy efficiency (due to the effects of concentration polarization).

Can Net Energy be Extracted by Mixing River Water with Seawater? NPG studies thus far have only been conducted under ideal conditions, neglecting important practical considerations which could significantly detract from the overall process viability. Moreover, previous studies have focused on measurement of the obtained power density—a parameter that determines the required membrane area or NPG system size for a specific power generation—but failed to quantify the energy efficiency and net extractable energy of an NPG system. The ultimate goal of NPG is to harness energy through the mixing of readily available source waters, most typically envisioned as the mixing of river water and seawater. While real waters pose the potential for severe membrane fouling and scaling,^{12,96} phenomena which compromise process performance in all membrane processes, NPG experiments have exclusively used synthetic pure salt solutions.^{48,49,51} In neglecting the fouling potential of real waters, pretreatment processes required to mitigate fouling associated performance degradation have also been overlooked.^{12,22} The required pretreatment processes consume a considerable amount of energy, thereby diminishing the net energy extracted from NPG operation.^{22,97} Energy is also inevitably dissipated in practical operation through pressure drops along the membrane module, further reducing the effective extractable energy.^{97,98}

To assess the practical viability of operating NPG with the mixing of river water and seawater, we estimate the net extractable energy, taking the inherent energy consumptions of pretreatment and pressure drops into account (Figure 6).^{22,97} Figure 6A presents a breakdown of the various specific energy components in an NPG system using high-performance

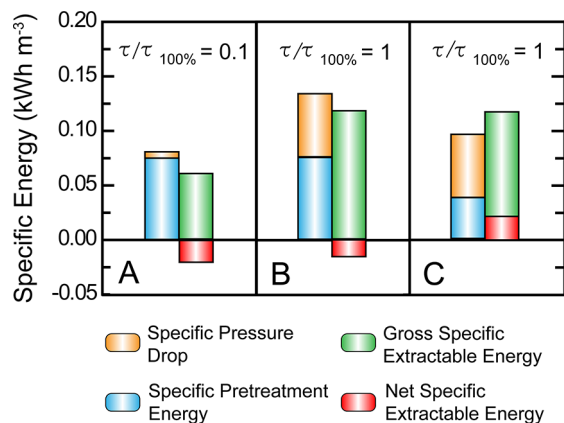


Figure 6. Breakdown of the specific energy in NPG operation with river water (1 mM) and seawater (600 mM). The gross specific extractable energy, specific pretreatment energy, specific pressure drops, and net specific extractable energy are represented by the green, blue, orange, and red bars, respectively. Different batch durations of (A) 10% and (B) 100% of the time required to achieve complete mixing were investigated. (C) Optimistic case of (B), in which the pretreatment energy requirement is halved. For (A) and (B), the specific pretreatment energies were assumed to be 0.1 kWh m⁻³ for seawater and 0.05 kWh m⁻³ for river water, resulting in an overall specific pretreatment energy of 0.075 kWh m⁻³ (*i.e.*, blue columns).²² Additional modeling parameters (*i.e.*, module dimensions, membrane properties, and operating conditions) are equal to those specified in scenario 2 of Figure 5B.

membranes and hydrodynamic conditions that minimize concentration polarization (Scenario 2 in Figure 5B). Note that the specified batch duration in Figure 6A represents a case of incomplete mixing (10% of the batch duration required for complete mixing), corresponding to an average power density of 1.97 W m⁻² (Figure 5B). While 0.06 kWh m⁻³ of gross energy is extracted (green bar) by the NPG system, the net specific energy, after accounting for the energetic penalties of pretreatment and pressure drops (details in Methods section), is -0.02 kWh m⁻³ (red bar). Notably, the negative sign signifies that the overall NPG process actually results in an overall consumption of energy, in contrast to the underlying goal of NPG to generate energy. This result is attributed to the very low extracted gross energy (0.06 kWh m⁻³) because of the limited mixing (*i.e.*, 10% of the batch duration required for complete mixing) and the relatively large specific pretreatment energy: 0.1 kWh m⁻³ for seawater and 0.05 kWh m⁻³ for river water,^{22,99,100} resulting in an overall specific pretreatment energy (per total volume of both solutions) of 0.075 kWh m⁻³ (blue bar). This analysis clearly shows that the energy required for pretreatment ultimately outweighs the energy extracted from the mixing of river water and seawater for the conditions simulated in Figure 6A.

As previously discussed and demonstrated in Figure 5B, the maximum extractable energy in NPG can be obtained by increasing the batch duration to achieve complete mixing. As shown in Figure 6B, increasing the batch duration results in higher (gross) extracted energy (0.12 kWh m⁻³, green bar), as expected. Nonetheless, even with complete mixing, the net specific energy remains negative (red bar). Though the increase in batch duration results in a greater amount of energy extracted from solution mixing, the energy losses from pressure drops in the module (orange bar) also drastically increase because of the large duration needed to achieve

complete mixing. Our results show that, regardless of NPG system size, the inevitable energetic costs of pretreatment and pressure drops make net energy extraction from the mixing of river water and seawater unfeasible.

Furthermore, we analyze the hypothetical scenario for complete mixing in which major technological innovations reduce the pretreatment energy consumption by a factor of 2 (Figure 6C). In this case, the net specific energy becomes positive though still very small in magnitude (0.02 kWh m⁻³). Such little extracted energy, however, is not practical for energy generation in a power plant. Assuming a full-scale NPG system producing 0.5 MW, equivalent to a small power plant, the flow rates of river water and seawater would be enormous (3.0 × 10⁵ m³ day⁻¹ for each). Considering initial capital costs, such as the membranes, pretreatment systems, pumps, and pipelines required to accommodate the huge flow rates (3.0 × 10⁵ m³ day⁻¹ for each river water and seawater), the construction of such a full-scale NPG system is not economically viable. Additionally, the major logistical and environmental challenges associated with the withdrawal of 3.0 × 10⁵ m³ day⁻¹ for each river water and seawater and the disposal of the 6.0 × 10⁵ m³ day⁻¹ resulting brine (produced after mixing) further detract from the feasibility of a full-scale NPG plant.

CONCLUSIONS

NPG continues to attract considerable attention, being perceived as a promising technology for harvesting blue energy. In this study, we rigorously assessed the performance and capabilities of NPG for a single nanopore, multipore membrane coupon, and full-scale system. In agreement with the literature, we observed ultrahigh power densities for a single nanopore, but upon moving to a multipore membrane coupon—for which ionic flux is substantially increased and concentration polarization must be considered—the power density drastically decreased. Accordingly, we emphasize that simple linear extrapolation of single-pore performance is not reflective of performance with multipore membranes, especially for membranes with high pore density. At the module scale, accounting for the variable salt concentration over the batch duration (as mixing proceeds) further reduced the achievable power density of NPG. Finally, practical operation of a full-scale NPG system mixing river water and seawater was considered. The energy demand of pretreatment processes and fluid flow related pressure drops were shown to outweigh the extractable energy by NPG, even with highly optimistic membrane properties and operating conditions. Upon significant reduction in pretreatment and pressure drop energy consumption, NPG achieves net energy generation, albeit an insignificant quantity which demands massive flow rates of river water and seawater to sustain a meaningful power generation. Thus, we conclude that NPG is not a feasible technology for net power production.

NPG's lack of viability stems from the insufficient amount of energy which can be extracted from the mixing of river and seawater—thermodynamically limited by the Gibbs energy of mixing for all blue energy technologies. Therefore, our conclusion that NPG is not of practical relevance is in agreement with viability analyses conducted of other blue energy technologies, namely, PRO and RED.^{12,19,22} However, it is critical to note that NPG's theoretical potential is severely limited, even in comparison to PRO and RED. This becomes apparent when considering the energy efficiency of NPG, which we demonstrated to be—at maximum—50%. RED,

which, in contrast to NPG, harnesses energy from the charge transfer of both cations and anions can theoretically achieve an energy efficiency of 100%. The overwhelming majority of NPG studies have focused on the development of cation-selective membranes, with little consideration of anion-selective transport. However, even in the case where an effective anion-selective nanoporous membrane is realized (and used in conjunction with a cation-selective nanoporous membrane), the energy efficiency of NPG would only approach that of RED.

Our analysis also revealed that improvement of nanopore material properties offers limited enhancement in overall NPG performance and cannot lead to process viability. Specifically, we showed that initial improvements of nanopore properties are expected to augment power density and energy efficiency, but beyond a particular threshold, further material advancements become relatively insignificant (Figure 4C). Thus, our findings are notably in agreement with the theme of a recent study which assessed the impact of advanced materials for desalination processes.¹⁰¹ We emphasize that material innovations are unable to overcome the shortcomings of NPG, with its limitations being thermodynamic in nature. Particularly, the maximum extractable energy in NPG (half the Gibbs energy of mixing)—regardless of material or operational improvements—is simply not substantial enough to compensate for the energy consumption of pretreatment and pressure drops and still be of practical value. We note that the energy consumption and the cost of the electrodes are not considered in our analysis, which would further compromise the practicality of NPG.

With the maximum extractable energy being a major limitation of NPG, highly concentrated brine solutions may be considered as a substitute for seawater, thereby effectively increasing the Gibbs free energy of mixing. However, such a configuration does not actually make NPG more practical, as the availability of brine resources, especially at the high volumetric flow rates required, is limited. The disposal of generated brine solutions (after mixing) would additionally be a logistical challenge and environmental concern, further detracting from process viability. Even in the case where such issues could be overcome and brine was used in place of seawater, PRO and RED would display superior energy efficiency compared to NPG, as previously discussed. Hence, this study overall demonstrated that NPG, despite being an area of considerable recent research focus, is a fundamentally inefficient and impractical blue energy harvesting technology.

METHODS

Dependence of Charge Density on pH. The charge density of the pore is influenced by local pH. In our model, we assume weak acid–base equilibria, using the dissociation constant (pK_a) of a monoprotic acid to describe the effects of pH on the surface charge density, σ ($C\ m^{-2}$).^{62,68,70,71} The acid dissociation constant, which is a nanopore property, determines the degree of protonation and is related to the surface charge density of the nanopore according to

$$\sigma = -e \frac{n}{1 + 10^{pK_a - pH}} \quad (14)$$

where n is the areal density of dissociable functional groups (m^{-2}) and e is the elementary charge (C).

The surface charge density is converted to volumetric charge density ($\text{mol}\ m^{-3}$), X , by

$$X = \frac{2\sigma}{FH} + X_f \quad (15)$$

where F is the Faraday constant ($C\ mol^{-1}$), H is the characteristic size (m), and X_f is the intrinsic charge density of the membrane material ($\text{mol}\ m^{-3}$). The characteristic size is the radius for a cylindrical pore or the height for a slit. The intrinsic charge, X_f is from strong acid functional groups which are not affected in relevant solution pH ranges. Unless otherwise specified, X_f is assumed to be zero throughout this study.

Modeling Ion Transport in a Nanopore. The ion transport in the nanopore is governed by the extended Nernst–Planck equation:

$$J_i = c_i u - D_i \left(\frac{dc_i}{dx} + z_i c_i \frac{d\varphi}{dx} \right) \quad (16)$$

where J_i is the ion flux of species i ($\text{mol}\ m^{-2}\ s^{-1}$), c_i is the species concentration ($\text{mol}\ m^{-3}$), u is the fluid velocity ($m\ s^{-1}$), D_i is the diffusion coefficient ($m^2\ s^{-1}$), z_i is ion valence, x is the distance from the pore entrance, and φ is the electric potential normalized by the thermal voltage (i.e., RT/F , which is 0.0256 V at room temperature). The average diffusion coefficient is used for both ions of the 1:1 electrolyte (i.e., $D_i = \sqrt{D_+ D_-}$). For the following derivation, we further normalize the variables in eq 16. The concentration and the volumetric charge density are normalized by C_0 ($\text{mol}\ m^{-3}$), which is a reference concentration ($1\ \text{mol}\ m^{-3}$). The coordinate from the pore entrance, x , is normalized by the length of the pore L_p (m), and the ion flux and flow velocity are normalized by DC_0/L_p .

The fluid velocity for a pore with a uniform potential across the radial direction can be calculated by^{102,103}

$$u = -\frac{1}{\Theta\alpha} \frac{dp_{h,p}}{dx} + \frac{X}{\Theta\alpha} \frac{d\varphi_{diff}}{dx} \quad (17)$$

Here, $p_{h,p}$ is the hydrostatic pressure inside the pore normalized by $C_0 RT$, Θ is a parameter to account for the cross-sectional geometry of the pore (e.g., 8 for a cylindrical pore), and α is the dimensionless viscosity parameter (equal to $\mu D / (C_0 R T H_p^2)$, where R is the gas constant, T is the absolute temperature, and μ is the fluid's dynamic viscosity).

Across the pore–solution interface, the chemical potential is continuous (i.e., the chemical potentials at the two sides of the interface are equal).^{82,85,104} We can represent the solute concentration in terms of osmotic pressure, by which the following relation for the pore–solution interfaces is derived:

$$p_{h,p} - \pi_p = p_{h,s} - \pi_s \quad (18)$$

where $p_{h,s}$ is the hydrostatic pressure of the solution outside the nanopore and π_p and π_s are the pore-side and solution-side osmotic pressures, respectively.

Inside the nanopore, the volumetric charge density is balanced by the ionic charge density, which is the difference between the cation (c_+) and the anion (c_-) concentrations:

$$c_+ - c_- + X = 0 \quad (19)$$

We note that the assumption of uniform potential in the radial direction is valid only when the pore size is relatively small causing the electrical double layers to overlap. However, it has been verified that the uniform potential model is numerically accurate as long as the Debye length is comparable to the pore size at one side of the pore.^{102,105}

The salt flux (J_s) is the sum of the cation and the anion fluxes, while the charge flux is the net ion flux (J_{ch}), equal to the difference of the cation and the anion fluxes. Accordingly, the fluxes are represented by the following equations:^{106,107}

$$J_s = J_+ + J_- \quad (20a)$$

$$J_s = c_{tot} u - \cosh(\xi) \frac{dc_{tot}}{dx} + (\cosh(\xi)X + \sinh(\xi)c_{tot}) \frac{d\varphi_{diff}}{dx} - \sinh(\xi) \frac{dX}{dx} \quad (20b)$$

$$J_{\text{ch}} = J_+ - J_- \quad (21a)$$

$$J_{\text{ch}} = -Xu + \sinh(\xi) \frac{dc_{\text{tot}}}{dx} - (\sinh(\xi)X + \cosh(\xi)c_{\text{tot}}) \frac{d\varphi_{\text{diff}}}{dx} + \cosh(\xi) \frac{dX}{dx} \quad (21b)$$

where J_+ and J_- are the normalized cation and anion ion fluxes, respectively, c_{tot} is the normalized total ion concentration (*i.e.*, $c_{\text{tot}} = c_+ + c_-$), X is the volumetric charge density normalized by C_0 , and $\xi = \ln(\sqrt{D_+/D_-})$ is a correction factor that accounts for the difference in the diffusion coefficients of the cation and anion. Notably, the cation and anion fluxes do not include the proton and the hydroxyl ions because their concentrations are substantially lower than the salt concentrations at both sides of the nanopore.

Next, we evaluate the boundary conditions at the two ends of the nanopore. As shown in Figure S7, Donnan potentials are established at each of the two pore–solution interfaces due to the selective transport of the cation over the anion. At the pore–solution interface, the ion concentration inside the nanopore is related to the concentration of the adjacent solution side by

$$c_{+,0} = c_{s,0} \exp(-\Delta\varphi_{D0}) \quad (22a)$$

$$c_{+,1} = c_{s,1} \exp(-\Delta\varphi_{D1}) \quad (22b)$$

$$c_{-,0} = c_{s,0} \exp(\Delta\varphi_{D0}) \quad (23a)$$

$$c_{-,1} = c_{s,1} \exp(\Delta\varphi_{D1}) \quad (23b)$$

where $c_{+,0}$, $c_{-,0}$, $c_{+,1}$, and $c_{-,1}$ are the normalized cation and anion concentrations in the nanopore on the high-concentration side and low-concentration side, respectively, and $c_{s,0}$ and $c_{s,1}$ are the normalized concentrations of the bulk solutions adjacent to the nanopore on the high and low-salinity sides, respectively. Accordingly, $\Delta\varphi_{D0}$ and $\Delta\varphi_{D1}$ are the Donnan potentials at the high-concentration and low-concentration side, respectively. Note that both $\Delta\varphi_{D0}$ and $\Delta\varphi_{D1}$ are negative with respect to the bulk solution outside the pore due to the negative surface charge of the pore as described Figure S7 of the Supporting Information.

With the nanopore being negatively charged, the proton concentration in the nanopore increases, causing the pH inside and outside the nanopore to differ. Assuming both solutions outside the nanopore have the same pH, the proton concentrations in the nanopore on the high-concentration side ($c_{\text{H}^+,0}$) and the low-concentration side ($c_{\text{H}^+,1}$) can be determined by

$$c_{\text{H}^+,0} = c_{\text{H}^+,s} \exp(-\Delta\varphi_{D0}) \quad (24a)$$

$$c_{\text{H}^+,1} = c_{\text{H}^+,s} \exp(-\Delta\varphi_{D1}) \quad (24b)$$

where $c_{\text{H}^+,s}$ is the concentration of protons in the bulk solution. Because the magnitude of the Donnan potential on the high-salinity side, $\Delta\varphi_{D0}$, is smaller than that on the low-salinity side, $\Delta\varphi_{D1}$, $c_{\text{H}^+,1}$ is larger than $c_{\text{H}^+,0}$. With the surface of the nanopore walls containing pH-dependent dissociable functional groups (*e.g.*, carboxylic acid groups), variable surface charge density is established along the pore length. Higher pH (*i.e.*, lower proton concentration), as is the case on the high-salinity end of the pore, favors acid dissociation and thereby a greater charge density.

It is important to note that not all ion transport constructively contributes to the ionic current. Specifically, co-ion transport through the pore is a parasitic current, which detracts from the current density. Hence, it is critical to maximize the ratio of the net ion flux, J_{ch} , to the total salt flux, J_s , which is defined as the selectivity (S):

$$S = J_{\text{ch}}/J_s \quad (25)$$

If the pore is uncharged, there is no selective partitioning of cations over anions, and the transport inside the pore for both types of ions is

the same; hence, J_{ch} and the selectivity would be zero. In contrast, a selectivity of unity can theoretically occur with highly charged pores in which only cations or anions are present.

Modeling Concentration Polarization. A simplified film boundary layer model is utilized to consider concentration polarization at the nanopore-based membrane surfaces. In the stagnant boundary layers, the salt and charge fluxes are determined by

$$J_s = -2D \frac{dc}{dx} \quad (26)$$

$$J_{\text{ch}} = -2Dc \frac{d\varphi}{dx} \quad (27)$$

For a given boundary layer thickness, L_{sdl} , the concentration and potential differences across the boundary layer can be described by

$$\Delta c = \frac{J_s L_{\text{sdl}}}{2D} \quad (28)$$

$$\Delta\varphi_{\text{h}} = \frac{J_{\text{ch}} L_{\text{sdl}}}{2D\Delta c} \ln \frac{c_{\text{b,h}}}{c_{\text{s,h}}} \quad (29)$$

$$\Delta\varphi_{\text{l}} = \frac{J_{\text{ch}} L_{\text{sdl}}}{2D\Delta c} \ln \frac{c_{\text{s,l}}}{c_{\text{b,l}}} \quad (30)$$

where Δc is the concentration difference across the boundary layer, $\Delta\varphi_{\text{h}}$ and $\Delta\varphi_{\text{l}}$ are the potential drops across the boundary layer on the high-salinity side and the low-salinity side, respectively, and $c_{\text{b,h}}$, $c_{\text{s,h}}$, $c_{\text{s,l}}$, and $c_{\text{b,l}}$ are the concentrations of the bulk solution on the high-salinity side, the membrane surface concentration on the high-salinity side, the membrane surface concentration on the low-salinity side, and the bulk solution on the low-salinity side, respectively. The concentrations near the surface of the nanopore-based membrane, $c_{\text{s,h}}$ and $c_{\text{s,l}}$ are therefore

$$c_{\text{s,h}} = c_{\text{b,h}} - \Delta c \quad (31)$$

$$c_{\text{s,l}} = c_{\text{b,l}} + \Delta c \quad (32)$$

Module-Scale Analysis. Extending the model to the module scale (*i.e.*, large membrane area in an NPG system) requires the definition of additional equations. First, the boundary layer thickness is estimated using the Sherwood number:¹⁰⁸

$$\text{Sh} = \frac{k d_{\text{h}}}{D} \quad (33)$$

where d_{h} is the hydraulic diameter and k is the mass transfer coefficient which is equal to D/L_{sdl} . Assuming the solutions adjacent to the nanopore–membrane flow through rectangular channels, the Sherwood number can be calculated based on the Reynolds number, Re , and Schmidt number, Sc , according to^{109,110}

$$\text{Sh} = 0.29\text{Re}^{0.5}\text{Sc}^{0.33} \quad (34)$$

The Reynolds number and the Schmidt number in eq 34 are defined as

$$\text{Re} = \frac{\rho v d_{\text{h}}}{\mu} \quad (35)$$

$$\text{Sc} = \frac{\mu}{\rho D} \quad (36)$$

where v is the longitudinal average flow velocity inside the module and ρ is the fluid density.

The module channel is discretized into m elements for both the high- and low-concentration sides of the membrane, with the salt flux in element m denoted as $J_{s,m}$. According to mass conservation, the bulk concentrations in element $m + 1$ are calculated by

$$c_{\text{h},m+1} = c_{\text{h},m} - \frac{J_{s,m} \tau}{L_{\text{sp}}} \quad (37)$$

$$c_{i,m+1} = c_{i,m} + \frac{J_{s,m} \tau}{L_{sp}} \quad (38)$$

where τ is the hydraulic residence time in the element and L_{sp} is the flow channel thickness.

In the module channel, we also consider the pressure drop due to fluid flow (ΔP), which is related to the flow velocity in the channel according to¹¹¹

$$\Delta P = f \frac{\rho v^2}{2d_h} L \quad (39)$$

where ρ is the fluid density, L is the length of the flow channel, and f is the Darcy friction factor (approximated as $24/Re$ for laminar flow in a fully wetted rectangular channel). Note that the pressure drop (ΔP) is equivalent to the specific energy loss (kWh m^{-3}).

ASSOCIATED CONTENT

Supporting Information

The Supporting Information is available free of charge at <https://pubs.acs.org/doi/10.1021/acsnano.0c08628>.

Schematic illustration of the multiscale process modeling hierarchy used to analyze NPG in this study (Figure S1); model validation with experimental data from NPG literature (Figure S2); optimal pore size of generating power from a single nanopore as a function of salt concentration ratio (Figure S3); intrinsic selectivity of a multi-nanopore membrane coupon as a function of pore density (Figure S4); effect of varying pore properties on the maximum power density (Figure S5); comparison of operation modes for module-scale NPG (Figure S6); illustration of ion transport through a cation-selective nanopore separating high-concentration and low-concentration solutions (Figure S7); summary of advanced materials used in NPG studies (Table S1) (PDF)

AUTHOR INFORMATION

Corresponding Author

Menachem Elimelech – Department of Chemical and Environmental Engineering, Yale University, New Haven, Connecticut 06520, United States; orcid.org/0000-0003-4186-1563; Email: menachem.elimelech@yale.edu

Authors

Li Wang – Department of Chemical and Environmental Engineering, Yale University, New Haven, Connecticut 06520, United States; orcid.org/0000-0002-5542-6696

Zhangxin Wang – Department of Chemical and Environmental Engineering, Yale University, New Haven, Connecticut 06520, United States

Sohum K. Patel – Department of Chemical and Environmental Engineering, Yale University, New Haven, Connecticut 06520, United States; orcid.org/0000-0001-5228-9449

Shihong Lin – Department of Civil and Environmental Engineering, Vanderbilt University, Nashville, Tennessee 37235-1831, United States; orcid.org/0000-0001-9832-9127

Complete contact information is available at: <https://pubs.acs.org/doi/10.1021/acsnano.0c08628>

Notes

The authors declare no competing financial interest.

ACKNOWLEDGMENTS

This work was supported by CENT, an Energy Frontier Research Center funded by the U.S. Department of Energy, Office of Science, Basic Energy Sciences, under Award No. DE-SC0019112.

REFERENCES

- (1) Isaacs, J. D.; Seymour, R. J. The Ocean as a Power Resource. *Int. J. Environ. Stud.* **1973**, *4*, 201–205.
- (2) Schaetzle, O.; Buisman, C. J. N. Salinity Gradient Energy: Current State and New Trends. *Engineering-Proc* **2015**, *1*, 164–166.
- (3) Tomabechi, K. Energy Resources in the Future. *Energies* **2010**, *3*, 686–695.
- (4) Norman, R. S. Water Salination: A Source of Energy. *Science* **1974**, *186*, 350.
- (5) Dai, A.; Trenberth, K. E. Estimates of Freshwater Discharge from Continents: Latitudinal and Seasonal Variations. *J. Hydrometeorol* **2002**, *3*, 660–687.
- (6) Nijmeijer, K.; Metz, S. Salinity Gradient Energy. In *Sustainability Science and Engineering*; Escobar, I. C., Schäfer, A. I., Eds.; Elsevier: Amsterdam, 2010; Vol. 2, Chapter 5, pp 95–139.
- (7) Ramon, G. Z.; Feinberg, B. J.; Hoek, E. M. V. Membrane-Based Production of Salinity-Gradient Power. *Energy Environ. Sci.* **2011**, *4*, 4423–4434.
- (8) Helfer, F.; Lemckert, C.; Anissimov, Y. G. Osmotic Power with Pressure Retarded Osmosis: Theory, Performance and Trends - A Review. *J. Membr. Sci.* **2014**, *453*, 337–358.
- (9) Sarp, S.; Li, Z.; Sathasivam, J. Pressure Retarded Osmosis (PRO): Past Experiences, Current Developments, and Future Prospects. *Desalination* **2016**, *389*, 2–14.
- (10) Yip, N. Y.; Elimelech, M. Thermodynamic and Energy Efficiency Analysis of Power Generation from Natural Salinity Gradients by Pressure Retarded Osmosis. *Environ. Sci. Technol.* **2012**, *46*, 5230–5239.
- (11) Post, J. W.; Hamelers, H. V. M.; Buisman, C. J. N. Energy Recovery from Controlled Mixing Salt and Fresh Water with a Reverse Electrodialysis System. *Environ. Sci. Technol.* **2008**, *42*, 5785–5790.
- (12) Yip, N. Y.; Vermaas, D. A.; Nijmeijer, K.; Elimelech, M. Thermodynamic, Energy Efficiency, and Power Density Analysis of Reverse Electrodialysis Power Generation with Natural Salinity Gradients. *Environ. Sci. Technol.* **2014**, *48*, 4925–4936.
- (13) Achilli, A.; Cath, T. Y.; Childress, A. E. Power Generation with Pressure Retarded Osmosis: An Experimental and Theoretical Investigation. *J. Membr. Sci.* **2009**, *343*, 42–52.
- (14) Han, G.; Zhang, S.; Li, X.; Chung, T. S. High Performance Thin Film Composite Pressure Retarded Osmosis (PRO) Membranes for Renewable Salinity-Gradient Energy Generation. *J. Membr. Sci.* **2013**, *440*, 108–121.
- (15) Li, X.; Zhang, S.; Fu, F. J.; Chung, T. S. Deformation and Reinforcement of Thin-Film Composite (TFC) Polyamide-Imide (PAI) Membranes for Osmotic Power Generation. *J. Membr. Sci.* **2013**, *434*, 204–217.
- (16) Vermaas, D. A.; Saakes, M.; Nijmeijer, K. Doubled Power Density from Salinity Gradients at Reduced Intermembrane Distance. *Environ. Sci. Technol.* **2011**, *45*, 7089–7095.
- (17) Skilhagen, S. E.; Dugstad, J. E.; Aaberg, R. J. Osmotic Power - Power Production Based on the Osmotic Pressure Difference between Waters with Varying Salt Gradients. *Desalination* **2008**, *220*, 476–482.
- (18) Tedesco, M.; Scalici, C.; Vaccari, D.; Cipollina, A.; Tamburini, A.; Micale, G. Performance of the First Reverse Electrodialysis Pilot Plant for Power Production from Saline Waters and Concentrated Brines. *J. Membr. Sci.* **2016**, *500*, 33–45.
- (19) Yip, N. Y.; Brogioli, D.; Hamelers, H. V. M.; Nijmeijer, K. Salinity Gradients for Sustainable Energy: Primer, Progress, and Prospects. *Environ. Sci. Technol.* **2016**, *50*, 12072–12094.
- (20) Straub, A. P.; Lin, S. H.; Elimelech, M. Module-Scale Analysis of Pressure Retarded Osmosis: Performance Limitations and

Implications for Full-Scale Operation. *Environ. Sci. Technol.* **2014**, *48*, 12435–12444.

(21) Lin, S. H.; Straub, A. P.; Elimelech, M. Thermodynamic Limits of Extractable Energy by Pressure Retarded Osmosis. *Energy Environ. Sci.* **2014**, *7*, 2706–2714.

(22) Straub, A. P.; Deshmukh, A.; Elimelech, M. Pressure-Retarded Osmosis for Power Generation from Salinity Gradients: Is It Viable? *Energy Environ. Sci.* **2016**, *9*, 31–48.

(23) Chung, H. W.; Banchik, L. D.; Swaminathan, J.; Lienhard, V. J. H. On the Present and Future Economic Viability of Stand-Alone Pressure-Retarded Osmosis. *Desalination* **2017**, *408*, 133–144.

(24) Gao, J.; Feng, Y. P.; Guo, W.; Jiang, L. Nanofluidics in Two-Dimensional Layered Materials: Inspirations from Nature. *Chem. Soc. Rev.* **2017**, *46*, 5400–5424.

(25) Wang, L. D.; Boutlier, M. S. H.; Kidambi, P. R.; Jang, D.; Hadjiconstantinou, N. G.; Karnik, R. Fundamental Transport Mechanisms, Fabrication and Potential Applications of Nanoporous Atomically Thin Membranes. *Nat. Nanotechnol.* **2017**, *12*, 509–522.

(26) Tarelho, J. P.G.; Soares dos Santos, M. P.; Ferreira, J. A.F.; Ramos, A.; Kopyl, S.; Kim, S. O.; Hong, S.; Kholkin, A. Graphene-Based Materials and Structures for Energy Harvesting with Fluids - A Review. *Mater. Today* **2018**, *21*, 1019–1041.

(27) Kong, X. Y.; Wen, L. P.; Jiang, L. Towards Practical Osmotic Energy Capture by a Layer-by-Layer Membrane. *Trends Chem.* **2020**, *2*, 180–182.

(28) Xiao, K.; Jiang, L.; Antonietti, M. Ion Transport in Nanofluidic Devices for Energy Harvesting. *Joule* **2019**, *3*, 2364–2380.

(29) Kim, D. K.; Duan, C. H.; Chen, Y. F.; Majumdar, A. Power Generation from Concentration Gradient by Reverse Electrodialysis in Ion-Selective Nanochannels. *Microfluid. Nanofluid.* **2010**, *9*, 1215–1224.

(30) Lee, S. W.; Kim, H. J.; Kim, D. K. Power Generation from Concentration Gradient by Reverse Electrodialysis in Dense Silica Membranes for Microfluidic and Nanofluidic Systems. *Energies* **2016**, *9*, 49.

(31) Kwak, S. H.; Kwon, S. R.; Baek, S.; Lim, S. M.; Joo, Y. C.; Chung, T. D. Densely Charged Polyelectrolyte-Stuffed Nanochannel Arrays for Power Generation from Salinity Gradient. *Sci. Rep.* **2016**, *6*, 26416.

(32) Hwang, J.; Kataoka, S.; Endo, A.; Daiguji, H. Enhanced Energy Harvesting by Concentration Gradient-Driven Ion Transport in SBA-15 Mesoporous Silica Thin Films. *Lab Chip* **2016**, *16*, 3824–3832.

(33) Chen, J.; Xin, W.; Kong, X.-Y.; Qian, Y.; Zhao, X.; Chen, W.; Sun, Y.; Wu, Y.; Jiang, L.; Wen, L. Ultrathin and Robust Silk Fibroin Membrane for High-Performance Osmotic Energy Conversion. *ACS Energy Lett.* **2020**, *5*, 742–748.

(34) Guo, W.; Cao, L.; Xia, J.; Nie, F.-Q.; Ma, W.; Xue, J.; Song, Y.; Zhu, D.; Wang, Y.; Jiang, L. Energy Harvesting with Single-Ion-Selective Nanopores: A Concentration-Gradient-Driven Nanofluidic Power Source. *Adv. Funct. Mater.* **2010**, *20*, 1339–1344.

(35) Liu, X.; He, M.; Calvani, D.; Qi, H. Y.; Gupta, K. B. S. S.; de Groot, H. J. M.; Sevink, G. J. A.; Buda, F.; Kaiser, U.; Schneider, G. F. Power Generation by Reverse Electrodialysis in a Single-Layer Nanoporous Membrane Made from Core-Rim Polycyclic Aromatic Hydrocarbons. *Nat. Nanotechnol.* **2020**, *15*, 307–312.

(36) Balme, S.; Ma, T. J.; Balanzat, E.; Janot, J. M. Large Osmotic Energy Harvesting from Functionalized Conical Nanopore Suitable for Membrane Applications. *J. Membr. Sci.* **2017**, *544*, 18–24.

(37) Lin, C. Y.; Combs, C.; Su, Y. S.; Yeh, L. H.; Siwy, Z. S. Rectification of Concentration Polarization in Mesopores Leads to High Conductance Ionic Diodes and High Performance Osmotic Power. *J. Am. Chem. Soc.* **2019**, *141*, 3691–3698.

(38) Cao, L. X.; Guo, W.; Ma, W.; Wang, L.; Xia, F.; Wang, S. T.; Wang, Y. G.; Jiang, L.; Zhu, D. B. Towards Understanding the Nanofluidic Reverse Electrodialysis System: Well Matched Charge Selectivity and Ionic Composition. *Energy Environ. Sci.* **2011**, *4*, 2259–2266.

(39) Li, R. R.; Jiang, J. Q.; Liu, Q. Q.; Xie, Z. Q.; Zhai, J. Hybrid Nanochannel Membrane Based on Polymer/MOF for High-Perform-

ance Salinity Gradient Power Generation. *Nano Energy* **2018**, *53*, 643–649.

(40) Zhang, Z.; He, L.; Zhu, C. C.; Qian, Y. C.; Wen, L. P.; Jiang, L. Improved Osmotic Energy Conversion in Heterogeneous Membrane Boosted by Three-Dimensional Hydrogel Interface. *Nat. Commun.* **2020**, *11*, 875.

(41) Zhang, Z.; Sui, X.; Li, P.; Xie, G. H.; Kong, X. Y.; Xiao, K.; Gao, L. C.; Wen, L. P.; Jiang, L. Ultrathin and Ion-Selective Janus Membranes for High-Performance Osmotic Energy Conversion. *J. Am. Chem. Soc.* **2017**, *139*, 8905–8914.

(42) Zhang, Z.; Kong, X. Y.; Xiao, K.; Liu, Q.; Xie, G. H.; Li, P.; Ma, J.; Tian, Y.; Wen, L. P.; Jiang, L. Engineered Asymmetric Heterogeneous Membrane: A Concentration-Gradient-Driven Energy Harvesting Device. *J. Am. Chem. Soc.* **2015**, *137*, 14765–14772.

(43) Xin, W. W.; Zhang, Z.; Huang, X. D.; Hu, Y. H.; Zhou, T.; Zhu, C. C.; Kong, X. Y.; Jiang, L.; Wen, L. P. High-Performance Silk-Based Hybrid Membranes Employed for Osmotic Energy Conversion. *Nat. Commun.* **2019**, *10*, 3876.

(44) Sui, X.; Zhang, Z.; Li, C.; Gao, L. C.; Zhao, Y.; Yang, L. J.; Wen, L. P.; Jiang, L. Engineered Nanochannel Membranes with Diode-Like Behavior for Energy Conversion over a Wide pH Range. *ACS Appl. Mater. Interfaces* **2019**, *11*, 23815–23821.

(45) Xiao, K.; Giusto, P.; Wen, L. P.; Jiang, L.; Antonietti, M. Nanofluidic Ion Transport and Energy Conversion through Ultrathin Free-Standing Polymeric Carbon Nitride Membranes. *Angew. Chem., Int. Ed.* **2018**, *57*, 10123–10126.

(46) Cheng, H. F.; Zhou, Y.; Feng, Y. P.; Geng, W. X.; Liu, Q. F.; Guo, W.; Jiang, L. Electrokinetic Energy Conversion in Self-Assembled 2D Nanofluidic Channels with Janus Nanobuilding Blocks. *Adv. Mater.* **2017**, *29*, 1700177.

(47) Fu, Y. J.; Guo, X.; Wang, Y. H.; Wang, X. W.; Xue, J. M. An Atomically-Thin Graphene Reverse Electrodialysis System for Efficient Energy Harvesting from Salinity Gradient. *Nano Energy* **2019**, *57*, 783–790.

(48) Feng, J. D.; Graf, M.; Liu, K.; Ovchinnikov, D.; Dumcenco, D.; Heiranian, M.; Nandigana, V.; Aluru, N. R.; Kis, A.; Radenovic, A. Single-Layer MoS₂ Nanopores as Nanopower Generators. *Nature* **2016**, *536*, 197–200.

(49) Siria, A.; Poncharal, P.; Bianco, A. L.; Fulcrand, R.; Blase, X.; Purcell, S. T.; Bocquet, L. Giant Osmotic Energy Conversion Measured in a Single Transmembrane Boron Nitride Nanotube. *Nature* **2013**, *494*, 455–458.

(50) Graf, M.; Lihter, M.; Unuchek, D.; Sarathy, A.; Leburton, J. P.; Kis, A.; Radenovic, A. Light-Enhanced Blue Energy Generation Using MoS₂ Nanopores. *Joule* **2019**, *3*, 1549–1564.

(51) Hong, S.; Ming, F. W.; Shi, Y.; Li, R. Y.; Kim, I. S.; Tang, C. Y. Y.; Alshareef, H. N.; Wang, P. Two-Dimensional Ti₃C₂T_x Mxene Membranes as Nanofluidic Osmotic Power Generators. *ACS Nano* **2019**, *13*, 8917–8925.

(52) Cao, L. X.; Wen, Q.; Feng, Y. P.; Ji, D. Y.; Li, H.; Li, N.; Jiang, L.; Guo, W. On the Origin of Ion Selectivity in Ultrathin Nanopores: Insights for Membrane-Scale Osmotic Energy Conversion. *Adv. Funct. Mater.* **2018**, *28*, 1804189.

(53) Macha, M.; Marion, S.; Nandigana, V. V. R.; Radenovic, A. 2D Materials as an Emerging Platform for Nanopore-Based Power Generation. *Nat. Rev. Mater.* **2019**, *4*, 588–605.

(54) Siria, A.; Bocquet, M. L.; Bocquet, L. New Avenues for the Large-Scale Harvesting of Blue Energy. *Nat. Rev. Chem.* **2017**, *1*, 0091.

(55) Vlassiuk, I.; Smirnov, S.; Siwy, Z. Ionic Selectivity of Single Nanochannels. *Nano Lett.* **2008**, *8*, 1978–1985.

(56) Zhang, L.; Biesheuvel, P. M.; Ryzhkov, I. I. Theory of Ion and Water Transport in Electron-Conducting Membrane Pores with pH-Dependent Chemical Charge. *Phys. Rev. Appl.* **2019**, *12*, 014039.

(57) Geise, G. M.; Cassidy, H. J.; Paul, D. R.; Logan, B. E.; Hickner, M. A. Specific Ion Effects on Membrane Potential and the Permselectivity of Ion Exchange Membranes. *Phys. Chem. Chem. Phys.* **2014**, *16*, 21673–21681.

(58) Strathmann, H. *Introduction to Membrane Science and Technology*; Wiley-VCH: Weinheim, Germany, 2011.

- (59) Marbach, S.; Bocquet, L. Osmosis, from Molecular Insights to Large-Scale Applications. *Chem. Soc. Rev.* **2019**, *48*, 3102–3144.
- (60) Bocquet, L.; Charlaix, E. Nanofluidics, from Bulk to Interfaces. *Chem. Soc. Rev.* **2010**, *39*, 1073–1095.
- (61) Stein, D.; Kruithof, M.; Dekker, C. Surface-Charge-Governed Ion Transport in Nanofluidic Channels. *Phys. Rev. Lett.* **2004**, *93*, 035901.
- (62) Biesheuvel, P. M.; Bazant, M. Z. Analysis of Ionic Conductance of Carbon Nanotubes. *Phys. Rev. E: Stat. Phys., Plasmas, Fluids, Relat. Interdiscip. Top.* **2016**, *94*, 050601.
- (63) Fan, R.; Huh, S.; Yan, R.; Arnold, J.; Yang, P. D. Gated Proton Transport in Aligned Mesoporous Silica Films. *Nat. Mater.* **2008**, *7*, 303–307.
- (64) Tagliazucchi, M.; Rabin, Y.; Szleifer, I. Transport Rectification in Nanopores with Outer Membranes Modified with Surface Charges and Polyelectrolytes. *ACS Nano* **2013**, *7*, 9085–9097.
- (65) Fair, J. C.; Osterle, J. F. Reverse Electrodialysis in Charged Capillary Membranes. *J. Chem. Phys.* **1971**, *54*, 3307.
- (66) Ali, M.; Yameen, B.; Cervera, J.; Ramirez, P.; Neumann, R.; Ensinger, W.; Knoll, W.; Azzaroni, O. Layer-by-Layer Assembly of Polyelectrolytes into Ionic Current Rectifying Solid-State Nanopores: Insights from Theory and Experiment. *J. Am. Chem. Soc.* **2010**, *132*, 8338–8348.
- (67) Vlassioulis, I.; Apel, P. Y.; Dmitriev, S. N.; Healy, K.; Siwy, Z. S. Versatile Ultrathin Nanoporous Silicon Nitride Membranes. *Proc. Natl. Acad. Sci. U. S. A.* **2009**, *106*, 21039–21044.
- (68) Jiang, Z. J.; Stein, D. Electrofluidic Gating of a Chemically Reactive Surface. *Langmuir* **2010**, *26*, 8161–8173.
- (69) Mei, L. J.; Yeh, L. H.; Qian, S. Z. Gate Modulation of Proton Transport in a Nanopore. *Phys. Chem. Chem. Phys.* **2016**, *18*, 7449–7458.
- (70) van der Heyden, F. H. J.; Stein, D.; Dekker, C. Streaming Currents in a Single Nanofluidic Channel. *Phys. Rev. Lett.* **2005**, *95*, 116104.
- (71) Andersen, M. B.; van Soestbergen, M.; Mani, A.; Bruus, H.; Biesheuvel, P. M.; Bazant, M. Z. Current-Induced Membrane Discharge. *Phys. Rev. Lett.* **2012**, *109*, 108301.
- (72) Ramirez, P.; Alcaraz, A.; Mafe, S. Effects of pH on Ion Transport in Weak Amphoteric Membranes. *J. Electroanal. Chem.* **1997**, *436*, 119–125.
- (73) Ramirez, P.; Mafe, S.; Tanioka, A.; Saito, K. Modelling of Membrane Potential and Ionic Flux in Weak Amphoteric Polymer Membranes. *Polymer* **1997**, *38*, 4931–4934.
- (74) Takagi, R.; Nakagaki, M. Ionic Dialysis through Amphoteric Membranes. *Sep. Purif. Technol.* **2003**, *32*, 65–71.
- (75) Yang, K. L.; Ying, T. Y.; Yiacoymi, S.; Tsouris, C.; Vittoratos, E. S. Electrosorption of Ions from Aqueous Solutions by Carbon Aerogel: An Electrical Double-Layer Model. *Langmuir* **2001**, *17*, 1961–1969.
- (76) Hou, C. H.; Taboada-Serrano, P.; Yiacoymi, S.; Tsouris, C. Electrosorption Selectivity of Ions from Mixtures of Electrolytes inside Nanopores. *J. Chem. Phys.* **2008**, *129*, 224703.
- (77) Boon, N.; van Roij, R. 'Blue Energy' from Ion Adsorption and Electrode Charging in Sea and River Water. *Mol. Phys.* **2011**, *109*, 1229–1241.
- (78) Jiang, C. Y.; Wang, X. Y.; Gunawidjaja, R.; Lin, Y. H.; Gupta, M. K.; Kaplan, D. L.; Naik, R. R.; Tsukruk, V. V. Mechanical Properties of Robust Ultrathin Silk Fibroin Films. *Adv. Funct. Mater.* **2007**, *17*, 2229–2237.
- (79) Gao, J.; Guo, W.; Feng, D.; Wang, H. T.; Zhao, D. Y.; Jiang, L. High-Performance Ionic Diode Membrane for Salinity Gradient Power Generation. *J. Am. Chem. Soc.* **2014**, *136*, 12265–12272.
- (80) Fan, H. Q.; Yip, N. Y. Elucidating Conductivity-Permselectivity Tradeoffs in Electrodialysis and Reverse Electrodialysis by Structure-Property Analysis of Ion-Exchange Membranes. *J. Membr. Sci.* **2019**, *573*, 668–681.
- (81) McCutcheon, J. R.; Elimelech, M. Influence of Concentrative and Dilutive Internal Concentration Polarization on Flux Behavior in Forward Osmosis. *J. Membr. Sci.* **2006**, *284*, 237–247.
- (82) Mulder, M. *Basic Principles of Membrane Technology*; Kluwer Academic Publishers: Dordrecht, The Netherlands, 1996.
- (83) Kim, S.; Hoek, E. M. V. Modeling Concentration Polarization in Reverse Osmosis Processes. *Desalination* **2005**, *186*, 111–128.
- (84) Patel, R. D.; Lang, K. C.; Miller, I. F. Polarization in Ion-Exchange Membrane Electrodialysis. *Ind. Eng. Chem. Fundam.* **1977**, *16*, 340–348.
- (85) Baker, R. W. *Membrane Technology and Applications*, 3rd ed.; Wiley: West Sussex, UK, 2012.
- (86) Su, J. J.; Ji, D. Y.; Tang, J. L.; Li, H.; Feng, Y. P.; Cao, L. X.; Jiang, L.; Guo, W. Anomalous Pore-Density Dependence in Nanofluidic Osmotic Power Generation. *Chin. J. Chem.* **2018**, *36*, 417–420.
- (87) Secchi, E.; Nigues, A.; Jubin, L.; Siria, A.; Bocquet, L. Scaling Behavior for Ionic Transport and Its Fluctuations in Individual Carbon Nanotubes. *Phys. Rev. Lett.* **2016**, *116*, 154501.
- (88) Yeh, L. H.; Zhang, M. K.; Qian, S. Z. Ion Transport in a pH-Regulated Nanopore. *Anal. Chem.* **2013**, *85*, 7527–7534.
- (89) Gonzalez, A.; Grageda, M.; Ushak, S. Assessment of Pilot-Scale Water Purification Module with Electrodialysis Technology and Solar Energy. *Appl. Energy* **2017**, *206*, 1643–1652.
- (90) Bejan, A. *Advanced Engineering Thermodynamics*, 2nd ed.; Wiley: Hoboken, NJ, 1997; p 850.
- (91) Wang, L.; Violet, C.; DuChanois, R. M.; Elimelech, M. Derivation of the Theoretical Minimum Energy of Separation of Desalination Processes. *J. Chem. Educ.* **2020**, *97*, 4361–4369.
- (92) Vermaas, D. A.; Saakes, M.; Nijmeijer, K. Power Generation Using Profiled Membranes in Reverse Electrodialysis. *J. Membr. Sci.* **2011**, *385*, 234–242.
- (93) Logan, B. E.; Elimelech, M. Membrane-Based Processes for Sustainable Power Generation Using Water. *Nature* **2012**, *488*, 313–319.
- (94) Lin, S. H. Energy Efficiency of Desalination: Fundamental Insights from Intuitive Interpretation. *Environ. Sci. Technol.* **2019**, *54*, 76–84.
- (95) Patel, S. K.; Qin, M.; Walker, W. S.; Elimelech, M. Energy Efficiency of Electro-Driven Brackish Water Desalination: Electrodialysis Significantly Outperforms Membrane Capacitive Deionization. *Environ. Sci. Technol.* **2020**, *54*, 3663–3677.
- (96) Vermaas, D. A.; Kunteng, D.; Saakes, M.; Nijmeijer, K. Fouling in Reverse Electrodialysis under Natural Conditions. *Water Res.* **2013**, *47*, 1289–1298.
- (97) Wang, Z. X.; Hou, D. Y.; Lin, S. H. Gross vs. Net Energy: Towards a Rational Framework for Assessing the Practical Viability of Pressure Retarded Osmosis. *J. Membr. Sci.* **2016**, *503*, 132–147.
- (98) Kim, Y. C.; Kim, Y.; Oh, D.; Lee, K. H. Experimental Investigation of a Spiral-Wound Pressure-Retarded Osmosis Membrane Module for Osmotic Power Generation. *Environ. Sci. Technol.* **2013**, *47*, 2966–2973.
- (99) *Seawater Desalination Power Consumption*; WaterReuse Association: Arlington, VA, 2011.
- (100) Plappally, A. K.; Lienhard, J. H. Energy Requirements for Water Production, Treatment, End Use, Reclamation, and Disposal. *Renewable Sustainable Energy Rev.* **2012**, *16*, 4818–4848.
- (101) Patel, S. K.; Ritt, C. L.; Deshmukh, A.; Wang, Z.; Qin, M.; Epsztein, R.; Elimelech, M. The Relative Insignificance of Advanced Materials in Enhancing the Energy Efficiency of Desalination Technologies. *Energy Environ. Sci.* **2020**, *13*, 1694.
- (102) Peters, P. B.; van Roij, R.; Bazant, M. Z.; Biesheuvel, P. M. Analysis of Electrolyte Transport through Charged Nanopores. *Phys. Rev. E: Stat. Phys., Plasmas, Fluids, Relat. Interdiscip. Top.* **2016**, *93*, 053108.
- (103) Kang, Y. J.; Yang, C.; Huang, X. Y. Analysis of AC-Driven Electroosmotic Flow in a Microchannel Packed with Microspheres. *NSTI Nanotech 2004, Technical Proceedings* **2004**, *1*, 308–311.
- (104) Wijmans, J. G.; Baker, R. W. The Solution-Diffusion Model - A Review. *J. Membr. Sci.* **1995**, *107*, 1–21.

(105) Tian, H. H.; Zhang, L.; Wang, M. R. Applicability of Donnan Equilibrium Theory at Nanochannel-Reservoir Interfaces. *J. Colloid Interface Sci.* **2015**, *452*, 78–88.

(106) Catalano, J.; Hamelers, H. V. M.; Bienten, A.; Biesheuvel, P. M. Revisiting Morrison and Osterle 1965: The Efficiency of Membrane-Based Electrokinetic Energy Conversion. *J. Phys.: Condens. Matter* **2016**, *28*, 324001.

(107) Kristensen, M. B.; Bienten, A.; Tedesco, M.; Catalano, J. Counter-Ion Transport Number and Membrane Potential in Working Membrane Systems. *J. Colloid Interface Sci.* **2017**, *504*, 800–813.

(108) Kuroda, O.; Takahashi, S.; Nomura, M. Characteristics of Flow and Mass-Transfer Rate in an Electrodialyzer Compartment Including Spacer. *Desalination* **1983**, *46*, 225–232.

(109) Geraldes, V.; Afonso, M. D. Limiting Current Density in the Electrodialysis of Multi-Ionic Solutions. *J. Membr. Sci.* **2010**, *360*, 499–508.

(110) Wright, N. C.; Shah, S. R.; Amrose, S. E.; Winter, A. G. A Robust Model of Brackish Water Electrodialysis Desalination with Experimental Comparison at Different Size Scales. *Desalination* **2018**, *443*, 27–43.

(111) Chanson, H. Fundamentals of Open Channel Flows. In *Environmental Hydraulics of Open Channel Flows*; Chanson, H., Ed.; Butterworth-Heinemann: Oxford, UK, 2004; pp 11–34.